SNO-STR-95-066

Data Analysis of ESC Counting for Ra and Rn

Jian-X. Wang
University of Guelph
December 7, 1995

1. Radon measurement in ESC

The electrostatic chamber measures radon in the following way: radon source is attached to and is then introduced into the ESC with media gas. In some case, as for measuring thorium and radium in the MnO_2 beads, the media gas is circulated in a closed loop of chamber and source.

Radon from source is decayed and about 3/4 of the daughter product, Po, are positively charged. These Po ions are collected onto a Si alpha detector by an electric field applied between the chamber and the detector. The detector detects the decays of Po and its further decay products.

Th chain:

$$^{224}\mathrm{Ra} \xrightarrow{t_{1/2}=3.64d} {}^{220}\mathrm{Rn} \xrightarrow{t_{1/2}=55.6m} {}^{216}\mathrm{Po} \xrightarrow{t_{1/2}=0.15s} {}^{212}\mathrm{Pb} \longrightarrow$$

$$\xrightarrow{t_{1/2}=10.64h} {}^{212}\mathrm{Bi} \xrightarrow{60.6m} {}^{212}\mathrm{Po} \xrightarrow{t_{1/2}=0.3\mu s} {}^{208}\mathrm{Pb}$$

$$^{212}\mathrm{Bi} \xrightarrow{t_{1/2}=60.0m} {}^{308}\mathrm{Tl} \xrightarrow{t_{1/2}=30.6m} {}^{208}\mathrm{Pb}$$

U chain:

$$^{226}\mathrm{Ra} \xrightarrow{t_{1/2}=1602y} {}^{222}\mathrm{Rn} \xrightarrow{t_{1/2}=3.824d} {}^{218}\mathrm{Po} \xrightarrow{t_{1/2}=3.05m} {}^{214}\mathrm{Pb} \longrightarrow$$

$$\xrightarrow{t_{1/2}=26.8m} {}^{214}\mathrm{Bi} \xrightarrow{t_{1/2}=19.8m} {}^{214}\mathrm{Po} \xrightarrow{t_{1/2}=164\mu s} {}^{210}\mathrm{Pb} \xrightarrow{t_{1/2}=22y}$$

The following α decays should be observed in an acquired spectrum if both sources are presented:

	Radio nuclei	Energy (keV)
Thorium chain:	^{216}Po	6779
	^{212}Bi	6070
	^{212}Po	8786
Uranium chain:	^{218}Po	6003
	^{214}Po	7687

There should be three peaks from each chain. For the Th chain, the ^{216}Po is the direct decay product of ^{220}Rn. The calculation is straight forward and it is the main decay for ^{224}Ra-

^{220}Rn detection. Theoretically, the sum of ^{212}Bi and ^{212}Po will represent the ^{224}Ra-^{220}Rn activity. The relative long life of ^{212}Pb causes non-equilibrium between ^{216}Po and ^{212}Bi+Po for entire counting. This complicates calculation; ^{212}Bi peak is partly melted into ^{218}Po peak from uranium chain. The technique for separating two peaks for each other exists, but it's a time consuming task; ^{212}Po decays extremely fast with a half life of 0.3μs that is shorter than the electronics response time, some α is added into β from ^{212}Bi. This leaves a long tail on higher energy side on the peak.

For U chain, ^{218}Po peak is mainly used for ^{226}Ra-^{222}Rn measurement. It needs only about 20 to 30 minutes to form a secular equilibrium with ^{222}Rn. If high activity of ^{220}Rn presents, the uses of the ^{214}Po decay become essential. A few hours waiting are needed for the secular equilibrium between ^{222}Rn and ^{214}Po after the application of the electric field. ^{210}Po peak is not generally seen or used as the 22 year half life of ^{210}Pb makes this peak useless.

2 Formalism

For a decay chain

$$A_1 \xrightarrow{\lambda_1} A_2 \xrightarrow{\lambda_2} A_3 \xrightarrow{\lambda_3} A_4 \xrightarrow{\lambda_4} \cdots$$

At t=0, if only N_1 exist and all daughter products are zero, at time t, $N_n(t)$ can be written as:

$$N_n(t) - N_1(0)(\prod_{j=1}^{n-1}\lambda_j)\sum_{i=1}^{n}\frac{e^{-\lambda_i t}}{\prod_{k=1}^{n}(\lambda_{k(k\neq i)}-\lambda_i)}$$

2.1. ^{224}Ra analysis

From t=0 to t, there will be following amount of ^{224}Ra decayed:

$$D(t) = N_{Ra}(0) - N_{Ra}(t) = N_{Ra}(0) * (1 - exp^{-\lambda t})$$

It needs only a few minutes to obtain a secular equilibrium up to ^{216}Po. The latter should have exactly the same decay rate as ^{224}Ra. The number of counts in ^{216}Po alpha peak from t=0 to t is the product of D(t) and ε:

$$C(t) = \varepsilon * D(t) = \varepsilon * N_{Ra}(0) * (1 - exp^{-\lambda t})$$

This is the so called cumulated data. If C(t) and t are recorded, and ε is well known, the N_{Ra} can then be calculated with $N_{Ra}(0) = C(t) / (\varepsilon * (1 - exp^{-\lambda t}))$. If time can be recorded accurately, the error of $N_{Ra}(t)$ can be written as:

$$dN_{Ra}/N_{Ra} = dC(t)/C + d\varepsilon/\varepsilon$$

If the counting data between t_1 to t_2 is analyzed, $C(t_1 \rightarrow t_2)$ would be $C(t_2) - C(t_1)$:

$$C(t_1 \rightarrow t_2) = \varepsilon * N_{Ra}(0) * (\exp^{-\lambda t_1} - \exp^{-\lambda t_2})$$

This is so called differential data analysis. $N_{Ra}(0)$ and its error can be calculated in the same way as for cumulated data set. The differential data analysis is the correct analysis method for all Radon and Thoron measurements with ESC.

2.2. ^{226}Ra analysis

From t=0 to t, there will be:

$$D_{Ra} = N_{Ra}(0) * (1 - \exp^{-\lambda t})$$

^{226}Ra decayed and a same amount of ^{222}Rn has been produced. The amount of ^{222}Rn left at the end of time t should be:

$$N_{Rn}(t) = N_{Ra}\left(\frac{\lambda_1}{\lambda_2-\lambda_1}\exp^{-\lambda_1 t} + \frac{\lambda_1}{\lambda_1-\lambda_2}\exp^{-\lambda_2 t}\right)$$

where λ_1 is the decay constant of ^{226}Ra and λ_2 is that of ^{222}Rn. The difference is the number of Rn decayed from t=0 to t:

$$D_{Rn}(0 \rightarrow t) = D_{Ra}(0 \rightarrow t) - N_{Rn}(t) = N_{Ra}(0) * \left(1 - \exp^{-\lambda_1 t} - \left(\frac{\lambda_1}{\lambda_2-\lambda_1}\exp^{-\lambda_1 t} + \frac{\lambda_1}{\lambda_1-\lambda_2}\exp^{-\lambda_2 t}\right)\right)$$

As $\lambda_1 = 5*10^{-8}\ h^{-1}$ and $\lambda_2 = 7.5*10^{-3}\ h^{-1}$, and within our measurement time (<1000 hours), $\exp(-\lambda_1 t)$ will be always closed to 1.0, we can simplify $\lambda_1/(\lambda_2-\lambda_1)$ to λ_1/λ_2 and $\exp(-\lambda_1 t)$ to $1-\lambda_1 t$. It becomes:

$$D_{Rn}(0 \rightarrow t) = N_{Ra}(0) * \left(1 - (1-\lambda_1 t) - \frac{\lambda_1}{\lambda_2}(1 - \lambda_1 t - \exp^{-\lambda_2 t})\right)$$

or

$$D_{Rn}(0 \rightarrow t) = N_{Ra}(0) * \left(\lambda_1 t + \frac{\lambda_1^2}{\lambda_2} t - \frac{\lambda_1}{\lambda_2}(1 - \exp^{-\lambda_2 t})\right)$$

By ignoring the second order of λ_1 that is extremely small in any circumstance, the final formula is:

$$D_{Rn}(0 \rightarrow t) = A_{Ra}(0) * \left(t - \frac{1}{\lambda_2}(1 - \exp^{-\lambda_2 t})\right)$$

with the activity of ^{226}Ra, A_{Ra}. In practice, the Po decay is detected, and the efficiency of detection should be considered. Also if the ^{218}Po counts between t_1 and t_2 is analyzed, the following formula is used:

$$C_{Po}(t_1 \to t_2) = \varepsilon * A_{Ra}(0) * ((t_2 - t_1) - \frac{1}{\lambda_2}(\exp^{-\lambda_2 t_1} - \exp^{-\lambda_2 t_2}))$$

The error of A_{Ra} can be calculated in the same way as in the section 2.1. if time is recorded accurately.

2.3 Non-supported ^{222}Rn analysis

Non-supported ^{222}Rn can be Rn in air absorbed in beads or absorbed on surfaces of all components of the entire counting system. But its decay and counting is in the same way as ^{224}Ra. The formulation in the section 2.1 can be applied here by replacing the λ with that of ^{222}Rn.

2.4. Fitting of data set

In presence of non-supported ^{222}Rn, there would be two components in the same Po peak for ^{226}Ra data analysis. The counts from t_1 to t_2 can be written as:

$$C(t_1 \to t_2) = \varepsilon * A_{Ra}(0) * ((t_2 - t_1) - \frac{1}{\lambda}(\exp^{-\lambda t_1} - \exp^{-\lambda t_2})) + \varepsilon * N_{Rn}(0) * (\exp^{-\lambda t_1} - \exp^{-\lambda t_2})$$

At least a set of two $C(t_1 \text{->} t_2)$ of different time is needed for the two unknown $A_{Ra}(0)$ and $N_{Rn}(0)$. The longer the counting time is performed and the more data points are recorded, the better the result would be.

3. Two practical analysis

3.1. ^{214}Po peak replacing ^{218}Po peak

As the ^{212}Bi alpha has roughly the same energy of that of ^{218}Po, in presence of high ^{224}Ra activity, the analysis of ^{222}Rn from ^{218}Po decay becomes difficult. In this case, ^{214}Po decay is used for the analysis of U chain. But ^{214}Po is delayed by 26.8+19.8 minutes. We can prove that if t is longer enough, say 6 hours, all three nuclei ^{214}Po, ^{218}Po and ^{222}Rn will decay at the same rate. $[C(t_2)-C(t_1)]/\varepsilon$ would be number of decays of all three. We just consider the first t_1 at >6 hours from a data set of hundreds hour counting.

3.2. In presence of Th

MnO_2 beads can extract Th from water as well as Ra. As ^{226}Ra has a half life of 1602 years, the presence of ^{230}Th will not interfere the analysis at all. But the presence of ^{228}Th will. If we consider ^{228}Th as ^{226}Ra, and ^{224}Ra as ^{222}Rn in U chain, this is exactly the same situation in the section 2.4. We can say there is a supported ^{224}Ra and a non-supported ^{224}Ra. The same set of data can be fitted to obtain two unknown A_{Th} and N_{Ra} using:

$$C(t_1 \rightarrow t_2) = \varepsilon * A_{Th}(0) * ((t_2 - t_1) - \frac{1}{\lambda}(\exp^{-\lambda t_1} - \exp^{-\lambda t_2})) + \varepsilon * N_{Ra}(0) * (\exp^{-\lambda t_1} - \exp^{-\lambda t_2})$$

with the λ of ^{224}Ra.

4. Conclusion

Data analysis of Rn measurement is relatively easy comparing to the work. For an accurate radio activity in water result, some points should be emphasized:

1) The background of the counting system as well as the beads and the column must be kept as low as possible. The data analysis of the system BG is the same as described above. For U chain, ^{226}Ra and ^{222}Rn activities are measured although the latter is not interested. It can be vary largely depending on environment. For Th chain, ^{224}Ra component should not be seen in a BG counting unless the system is contaminated or it's from newly made beads.

2) The entire water radio assay procedure should be standardized. Amount of beads used in each column should be constant; beads drying time should be longer enough and constant. The radon detection efficiency of the ESC should be verified once a year by using extremely weak source.

3) System should be sealed as tight as possible. Significant pressure raise can cause efficiency drop during measurement. Then incorrect result will be obtain.

4) Counting time of each measurement should be at least 100 hours. A longer counting time is preferred.

Energy Response and PMT Backgrounds in SNO
SNO-STR-96-015

Mike Lay
Nuclear Physics Laboratory, Oxford

May 29, 1996

1 Introduction and Definitions

> A beginning is a time for taking care that the balances are correct.....
> ..... Princess Irulan, *The Manual of Muad'Dib* [1]

Given the above advice, it seems prudent to start with a few general notes and definitions:

- Energies are kinetic energies in MeV.
- N_{hits} is the number of hit tubes in an event.
- Unless otherwise stated, the true radius of an event has been used. This avoids any fitter dependant complications (see discussion in Section 2).
- The mean and width of the distributions have been calculated by fitting a Gaussian to the N_{hits} spectrum. Although this is a better measure than calculating the mean and RMS spread, it still has problems with the 10 hits threshold; low energy (2 and 3 MeV) events tend to be somewhat distorted by this. The effect of this is to decrease the width and increase the mean N_{hits}.
- SNOMAN 2_09 was used for this analysis (comparison with 2_08 and across the development in 2_09 shows the results to be stable).
- Where a point is given as the location of an event, the electrons are started at that point, where a radius is given the electrons are started in a thin spherically symmetric shell at that radius.
- The term "default detector configuration" refers to the default Monte Carlo configuration.

2 Energy Calibration

2.1 Default detector configuration (with and without NCDs)

The upper plot of Figure 1 shows the average N_{hits} for monoenergetic electrons and gammas as a function of the initial energy. The events were started uniformly throughout the D_2O. The lower plot of Figure 1 uses the same data, but shows N_{hits} per MeV. The energy response from neutron capture on D and Cl is also shown. Table 1 shows some sample values. There are several points to note:

800 473-7983

- The N_{hits} plot is roughly linear in the region 2-15 MeV. However, the fit is not particularly good (a χ^2 of $\sim$ 20 per degree of freedom). Extrapolating the line to 20 MeV leads to a substantial error, as can be seen from the figure. A much better fit is given by a quadratic (χ^2 of $\sim$ 1 per degree of freedom), which accounts for the fall off in N_{hits} at low energies (due to the increasing importance of the Cerenkov cutoff) and at higher energies (as the probability of a multiple strike on a tube becomes more important). The latter effect could presumably be dispensed with by looking at the number of photo-electrons rather than N_{hits}, but this has not yet been investigated. Due to the poor charge resolution of the PMTs, it is not clear that the summation of deposited charge would improve the energy resolution of the detector.

- The extracted numbers are remarkably robust with respect to assumptions. Analysing the data under three scenarios (namely all recorded events, all events reconstructing inside the D_2O and all events reconstructing within 1m of its initial point) showed mo statistically significant difference for either calibration or width. This suggests that the results herein should be relatively stable with respect to choice of fitter.

- The lower than expected energy response and greater width of the Chlorine gamma cascade is a result of the multiplicity of the gamma rays.

- The location of the event can have an effect in rare circumstances. Figure 2 shows the fit to the energy response of nCl events at the centre of the detector, analysed in two classes;all events and all events reconstructing inside 600 cm. The fits are virtually identical, as are fits made with other assumptions (such as only considering events which are reconstructed within 100 cm if the initial start point). Figure 3 shows the same analysis for events started at 590cm. Events for which some of the γs escape into the light water form a high energy shoulder on the plot, which then tends to distort the Gaussian fit. In general, this is not a problem, most events discussed in this section will not intrude into the light water, but it serves to highlight a potential pitfall.

- Errors are not shown in the figures. However, expected errors (for a 10,000 event sample) are $\sim$ 1% for the width and $\sim$ 0.1% for the mean.

Figure 4 shows the same plots but with the current SNOMAN (2.09) model of the NCDs inserted into the D_2O. As has been predicted in other studies, the response of the detector drops by about 15%, but the gross features are otherwise unaffected.

Figure 5 shows the percentage width as a function of initial energy with and without the NCDs. As expected, the NCDs increase the width of the N_{hits} spectrum. Readers should note that the calculation of the width at higher energies can be complicated by the production of neutrons which subsequently capture on a deuterium producing a small subset of events at $\sim$ 5 MeV. In Monte Carlo this can be avoided by the simple expedient of turning the photo-disintegration off, but this is not an easy option in the real detector! The width distributions have a functional form of roughly $1/\sqrt{T}$, where T is the kinetic energy, however, a better functional form is $P_1/\sqrt{T-P_3} - P_2$, where the coefficients are shown in Table 2.

2.1.1 Radial dependance

Table 3 shows a comparison of the mean N_{hits} and width as a function of radius. Without the NCDs present, the N_{hits} value only changes by about 6% - the drop at 599 cm reflects the fact that some of the electrons are entering the acrylic and producing less Čerenkov light.

The percentage width is stable to within statistical errors[1]. This is not the case with the NCDs included in the simulation. Here we see a strong dependence on radius in both the magnitude and the width of the distribution. The change in the magnitude may be explained by remembering that events which occur at the centre of the detector see a forest of NCDs regardless of orientation. Events that occur in the outer parts of the D_2O, heading out, see only a few NCDs, whilst those heading into the detector see the above noted forest. This can be shown to give rise to a higher average, and also illustrates why the width increases as a function of radial distance.

2.2 Directional dependance and NCDs

The much touted directional dependence that occurs with the introduction of the NCDs appears to be overstated (see Table 4), at least in the cases studied. The largest deviations noted were of order 1%[2]. This relative insignificance of this effect appears to be a result of multiple scattering and the large opening angle of the Cerenkov cone. At these energies, the concept of an electron travelling parallel or perpendicular to the length of the NCDs is not valid. The only effect of interest is that the width for events at 550cm does have a directional dependance, and one that would become more exaggerated if events at the edge of the detector headed out where compared with those headed in.

2.3 The effect of changing the detector configuration

The Table 5 shows the effect on the N_{hits} spectrum for various changes to the detector configuration. The width is not shown as it was found to scale with the mean N_{hits}. As can be seen from the table, all the effects noted cause a $1-2\%$ change in the mean N_{hits}, a change that seems to be essentially independent of the location of the event. The exception is the addition of the tiles, which has little effect. Combining the tiles and the belly plates gives rise to a roughly 1.5% drop in detector efficiency, regardless of energy. This means that the calibration figures given elsewhere in this report have a systematic overestimate on them.

2.4 Conclusions

SNOMAN is predicting ~ 10.5 hits per MeV under normal circumstances and ~ 8.7 hits with the NCDs in. These numbers have a systematic error of $\sim 1.5\%$ due to the presence in the real detector of the belly plates and sanded joints at the perimeter of the acrylic tiles. The number of hits is essentially linear with energy, though at 20 MeV a slight curvature is noted, arising from the increasing probability of multiple photons scoring a hit on the same phototube. The presence of the NCDs has a definite impact on the dependence of N_{hits} with radius, but little on the directional dependence of the calibration. The width of the distribution does carry a directional dependance. At low energies, the relation between N_{hits} and energy is non linear, due to the effects of the Cerenkov cutoff and the hardware threshold of ~ 10 hits.

3 PMT Backgrounds

To date only ^{214}Bi, ^{208}Tl and ^{210}Tl have been examined - these decays have the highest Q-values by some margin. The current status is shown in Table 6. The events were set up inside

[1] Errors of 0.1 % in the mean and 1% in the width are expected from a sample of 10,000 events.

[2] And it should be noted that this is using the actual initial direction of the electron. The uncertainty in the calculated direction in real data may serve to wash this out to some extent.

the PMT glass bulb, and the threshold was set at 30 hits for reasons of disk space. It should be noted that this distorts the spectrum near the threshold. The time fitter was used in the analysis (as a worst case estimator), and the number of hit phototubes used as an indicator of the energy[3]. The number of events per year was derived from assuming the tube's activity to be evenly distributed through the PMT glass bulb (the neck was ignored), taking a glass mass of 800g, and an average of the Guelph and Birkbeck measured activities, taken from [2]. Equilibrium conditions were assumed.

The numbers in Table 6 suggest that there are no PMT events above 5 *MeV* (the highest recorded energy was a single event at 53 hits[4], whilst the highest energy reconstructing into the D_2O was 45 hits, corresponding to $\sim$ 4.3 MeV). There are however, $\sim$ 1500 events per year reconstructing inside the D_2O with energies in the range 3-4 MeV, and roughly 200 events per year inside 4m. It should be noted that the statistics on these numbers is poor; most of the 200 events inside 4m come from the pair of ^{208}Tl events that reconstructed, multiplied by the scaling factor of 100.

The numbers are also strongly fitter dependent. The 'grid fitter' line of Table 6 shows a re-analysis of the ^{210}Tl data with the grid fitter. The number reconstructing into the D_2O falls by a factor of 2, though the tail of the distribution still goes out to a little over 40 hits. This is not to say that the grid fitter is the ideal tool for the job, but it does serve to highlight the fact that exact predictions of PMT beta-gammas are in the same league as tea-leaf reading. A factor of two error (from choice of fitter) in the predicted numbers of PMT beta-gammas would seem conservative.

The 'NCDs' line shows what happens when the NCDs are introduced into the detector. Essentially, the rate drops by a factor of 2, but the tail reconstructing into the D_2O still goes out to 42 hits; now roughly 5 MeV. No attempt has been made to apply the radially dependent energy calibration to the PMT beta-gammas. The average N_{hits} per MeV is higher in the outer part of the D_2O, where most of the beta-gammas reconstruct, which would serve to reduce this problem somewhat.

3.1 Conclusions

A study of the PMT beta gamma singles and doubles rates suggests that of order 1500 events per year will reconstruct into the D_2O over a threshold of 30 hits. This prediction for the number of events is subject to a number of caveats, the most important being that the quality of the fitter may reduce this by at least a factor of two, and that most of the predicted events come from the extrapolation of the ^{208}Tl run, which currently has exceptionally poor statistics. The distribution goes out to 45 hits, corresponding to approximately 4 MeV, and has no real impact on the study of solar neutrino events above a threshold of 5 MeV. It is not clear to the author whether this will have an impact on other, lower energy, studies.

The addition of the NCDs lowers the number of reconstructing events by a factor of approximately 2, but the tail still extends out to 42 hits, corresponding to approximately 5 MeV, and thus still of no real concern, at least for solar neutrino events.

[3] this is thought to be superior to looking at the number of photo-electrons as it avoids the smearing of the signal that the single photoelectron spectrum would add.

[4] The event rate is a strong function of N_{hits}. Whilst the maximum observed hits is only a guide to the end point, it is the author's (unproven) opinion that events more than a couple of N_{hits} higher than the numbers are very unlikely. There is no current evidence to support a long tail to high N_{hits}.

References

[1] F. Herbert, "Dune", NEL books (1965).

[2] R.J. Boardman, D.Phil thesis (Oxford 1992).

Event	Response (N_{hits})	Width (%)
5 MeV e^-	51.82	17.3
10 MeV e^-	105.3	12.9
nD	51.82	17.3
nCl	61.17	22.6

Table 1: Detector responses for sample event classes started isotropically in the D_2O.

Parameter	P_1	P_2	P_3
Electrons	42.85 ± 2.70	0.06 ± 0.57	0.25 ± 0.18
Gammas	54.82 ± 1.89	2.87 ± 0.42	0.25 ± 0.18
Electrons (NCDs)	44.36 ± 2.20	3.87 ± 0.46	-2.08 ± 0.35
Gammas (NCDs)	47.87 ± 3.53	2.45 ± 0.80	0.46 ± 0.35

Table 2: Parameters for fitted functional forms of the width.

List of Tables

List of Figures

Radius (cm)	No NCDs N_{hits}	No NCDs Width	With NCDs N_{hits}	With NCDs Width
0	50.63 (1.00)	8.50 (16.8)	41.33 (1.00)	7.35 (17.8)
100	50.92 (1.00)	8.67 (17.0)	40.13 (0.97)	7.52 (18.7)
200	51.81 (1.02)	8.60 (16.6)	41.18 (1.00)	7.85 (19.1)
300	52.69 (1.04)	8.83 (16.8)	42.49 (1.03)	8.29 (19.5)
400	53.67 (1.06)	9.07 (16.9)	44.28 (1.07)	8.91 (20.1)
500	53.71 (1.06)	9.12 (17.0)	46.30 (1.12)	9.51 (20.5)
550	53.36 (1.05)	9.09 (17.0)	47.25 (1.14)	9.65 (20.4)
590	52.98 (1.05)	9.06 (17.1)	47.40 (1.14)	9.76 (20.6)
599	50.51 (0.99)	8.36 (16.6)	46.18 (1.12)	9.14 (19.8)

Table 3: Mean and width of N_{hits} as a function of radial distribution. For the mean, the figures in brackets show the value relative to the first row. For the width columns, the number in brackets is the percentage width.

Directional Cosines	5 MeV N_{hits}	5 MeV Width	10 MeV N_{hits}	10 MeV Width
Events at (0,0,0)				
Isotropic	41.18 (1.000)	7.44	83.14 (1.000)	11.13
(0, 1, 0)	41.24 (1.001)	7.41	82.74 (0.995)	11.17
(0, 0, 1)	41.46 (1.007)	7.49	83.67 (1.006)	11.21
(special)	41.01 (0.996)	7.51	82.72 (0.995)	11.11
Events Isotropic in D_2O				
Isotropic	45.15 (1.000)	9.42	90.66 (1.000)	15.18
(0, 1, 0)	45.41 (1.005)	9.54	90.92 (1.003)	15.66
(0, 0, 1)	45.11 (0.999)	8.85	90.51 (0.998)	13.62
(special)	44.91 (0.995)	9.38	89.68 (0.989)	15.35
Events at 550 cm				
Isotropic	47.25 (1.000)	9.85	93.82 (1.000)	15.85
(0, 1, 0)	47.41 (1.003)	9.89	94.31 (1.005)	15.92
(0, 0, 1)	46.67 (0.988)	9.26	93.08 (0.992)	15.64
(special)	46.83 (0.991)	9.85	93.39 (0.995)	16.13

Table 4: Directional dependence for events started in the D_2O with energies of 5 and 10 MeV. The special distribution consists of events at 45° to the z-axis. The numbers in brackets show the ratio of N_{hits} to the angular isotropic case. NCDs are included in the simulation. Statistical errors on N_{hits} are $\sim 0.1\%$.

Energy:	5 MeV (1)	10 MeV (2)	10 MeV (3)	10 MeV (4)
Baseline	53.17 (1.000)	107.1 (1.000)	103.2 (1.000)	106.9 (1.000)
Attenuation - D_2O	51.55 (0.970)	104.1 (0.972)	100.6 (0.974)	104.1 (0.974)
Attenuation - Acrylic	51.57 (0.970)	104.1 (0.972)	100.6 (0.974)	104.1 (0.974)
Attenuation - H_2O	52.41 (0.986)	105.2 (0.982)	101.9 (0.987)	105.3 (0.985)
Full belly Plates	52.33 (0.984)	105.8 (0.988)	102.0 (0.988)	105.3 (0.985)
Tiles	53.11 (0.999)	106.7 (0.996)	103.2 (1.000)	106.9 (1.000)
Tiles and Plates	52.50 (0.987)	105.5 (0.985)	102.0 (0.988)	105.4 (0.986)

Table 5: Calibration changes under a number of circumstances. The electrons were started with an isotropic angular distribution. Runs (1) and (2) were started isotropically in the D_2O, Run (3) was started at the origin, Run (4) was started at 550 cm. The attenuation lines had the appropriate attenuation coefficient increased by 20% . Statistical errors on N_{hits} are $\sim 0.1\%$, and on the width are $\sim 1.2\%$.

Source	Rate (yr^{-1})	Run	In D_2O	In 4m	Total	Scale (yr^{-1})	In D_2O (yr^{-1})
			Time Fitter - PMT singles				
^{208}Tl	7.5E9	7.5E7	12(41)	2(37)	1328(47)	100	1200
^{210}Tl	3.9E7	3.9E7	157(43)	4(41)	7817(53)	1	157
^{214}Bi	1.9E11	1.0E7	0	0	21(41)	1.9E4	0
			Time Fitter - PMT doubles				
^{208}Tl:^{210}Tl	963	963	0	0	8(50)	1	0
^{214}Bi:^{210}Tl	2.4E4	2.4E4	13(43)	3(33)	118(45)	1	13
^{210}Tl:^{210}Tl	4	4	0	0	0	1	0
^{214}Bi:^{208}Tl	4.6E6	4.6E5	5(45)	3(40)	32(45)	10	50
^{214}Bi:^{214}Bi	1.1E8	1E7	10(38)	3(36)	109(46)	11	110
^{208}Tl:^{208}Tl	1.9E5	1.8E5	13(43)	3(33)	118(51)	1	13
			Grid Fitter				
^{210}Tl	3.9E7	3.9E7	74(41)	0	7817(53)	1	74
			NCDs				
^{210}Tl	3.9E7	3.9E7	81(42)	5(36)	2910(51)	1	81

Table 6: PMT $\beta - \gamma$ runs for single events and double coincidence events. Columns one and two show the source decay and the expected rate, columns 3 to 6 show the number of events run, the number reconstructed inside the D_2O and inside 4m, and the total number of events over threshold. Columns 7 and 8 show the scaling factor to 1 year, and the expected number of events reconstructing in the D_2O per year. The numbers in brackets are the maximum N_{hits} in any category, and are presented to give the flavour of how far the spectrum extends.

Measurement	^{238}U	^{232}Th
Guelph	47.6 ± 4.8	19.9 ± 2.5
Birkbeck	38.8 ± 4.6	10.1 ± 1.5
Average	43.2	15.0

Table 7: Phototube activity measurements given in ppb by mass.

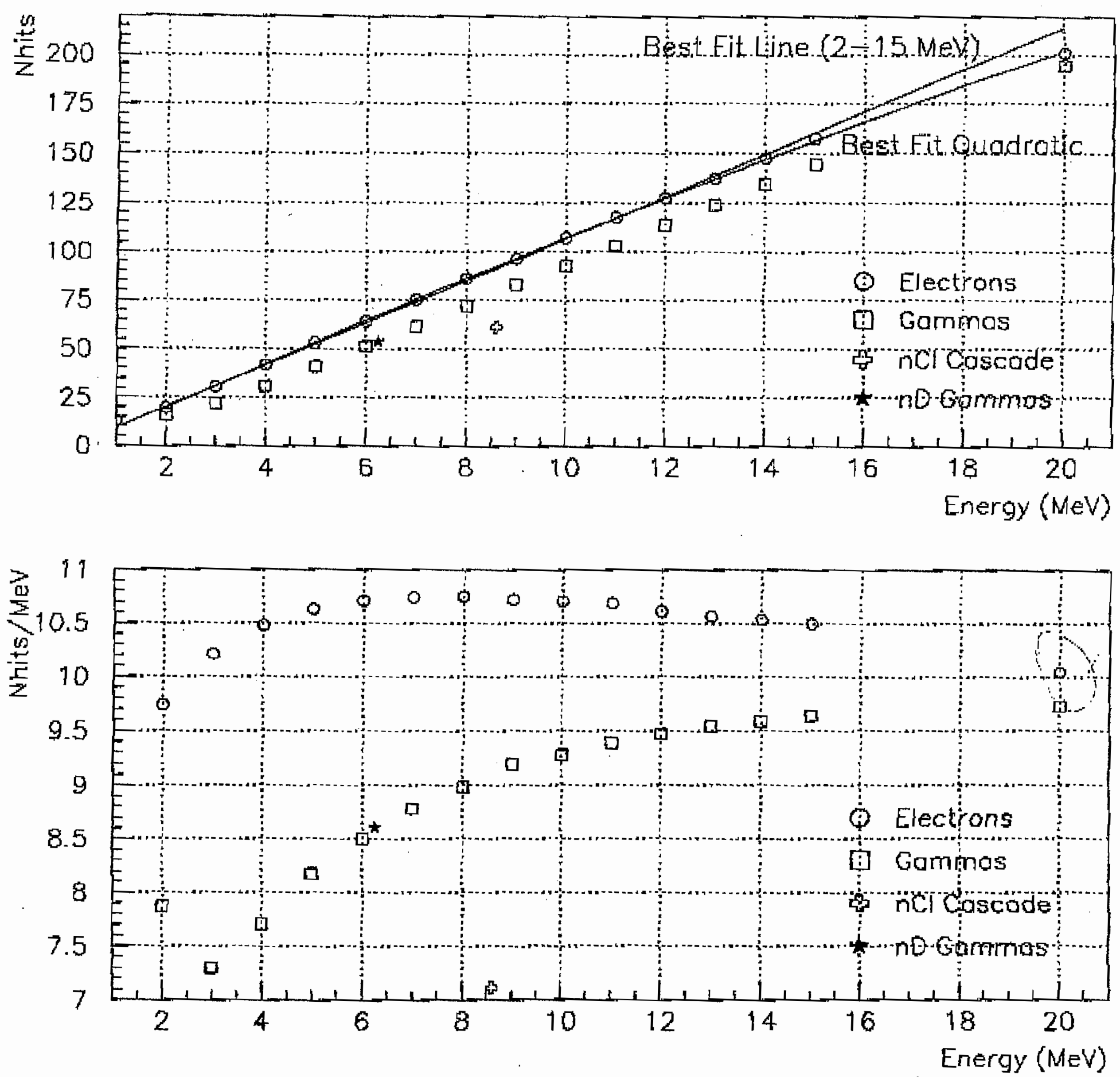

Figure 1: SNO calibration as a function of energy. Electrons isotropically in the D_2O, no NCDs.

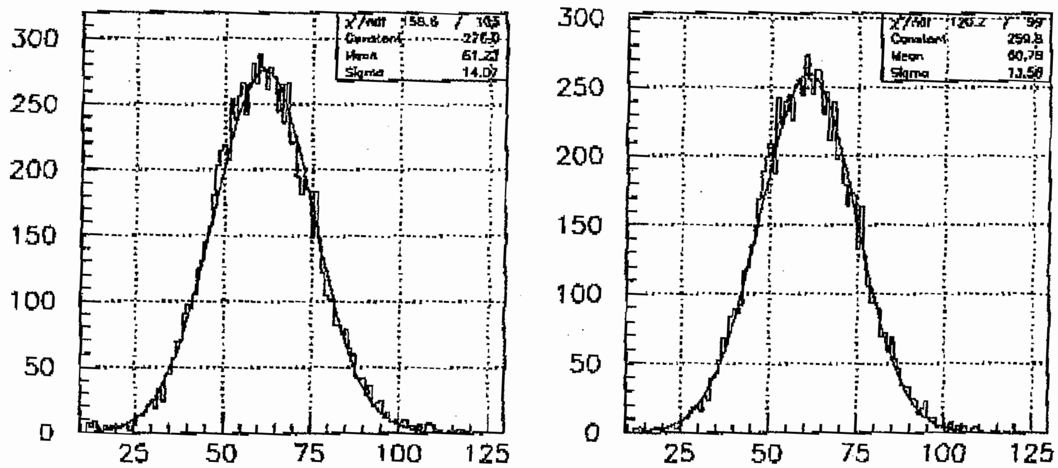

Figure 2: Gaussian fits to the N_{hits} response for nCl γ cascades isotropically generated in the D_2O. See text.

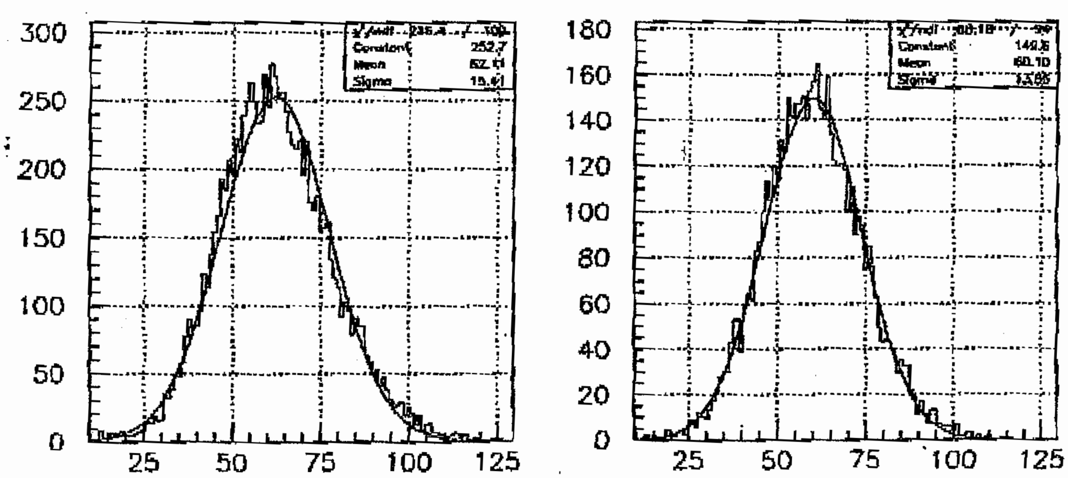

Figure 3: Gaussian fits to the N_{hits} response for nCl γ cascades generated at a radius of 590 cm in the D_2O. See text.

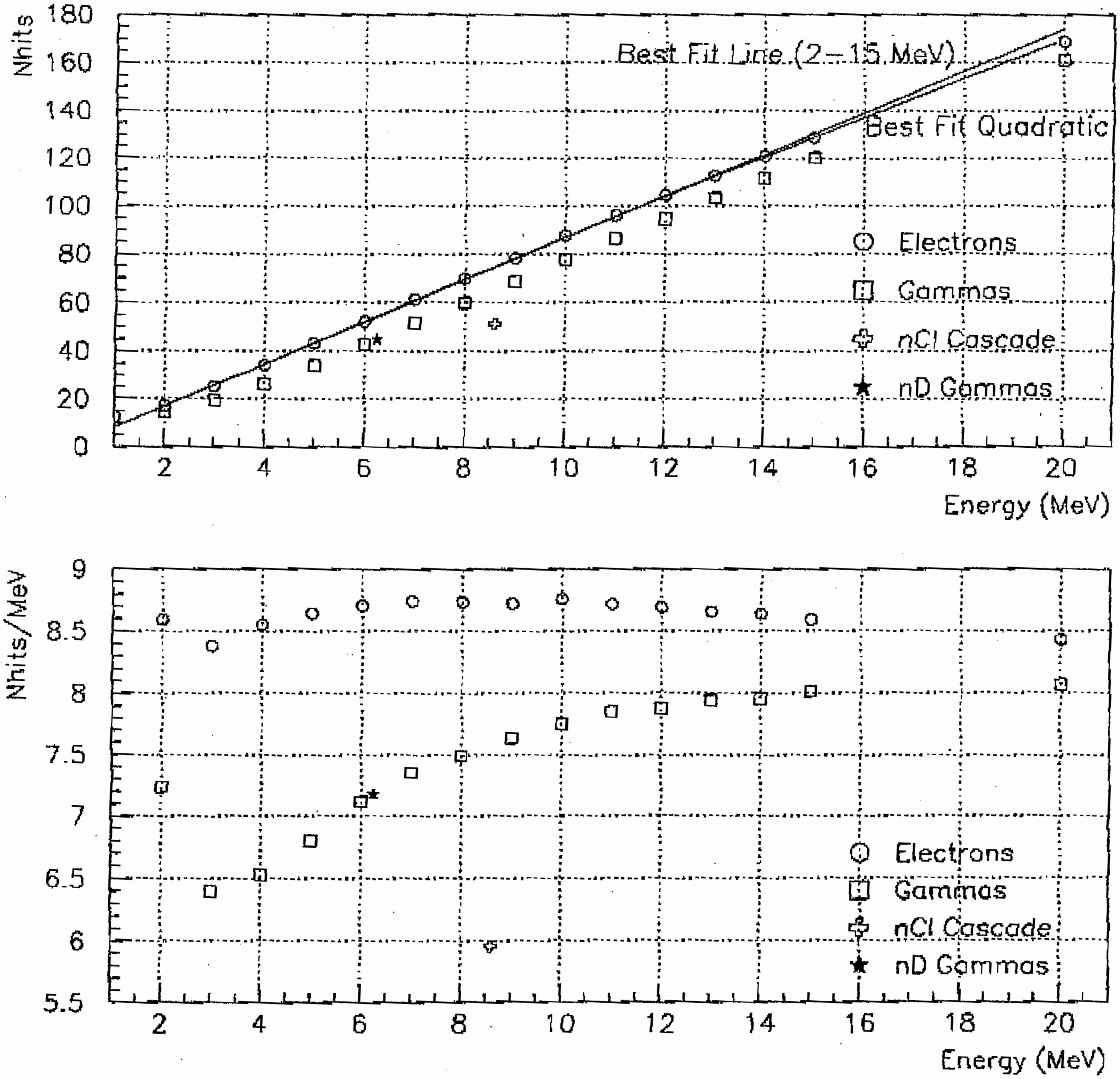

Figure 4: SNO calibration as a function of energy for electrons created isotropically in the D_2O. The NCDs are included in the simulation.

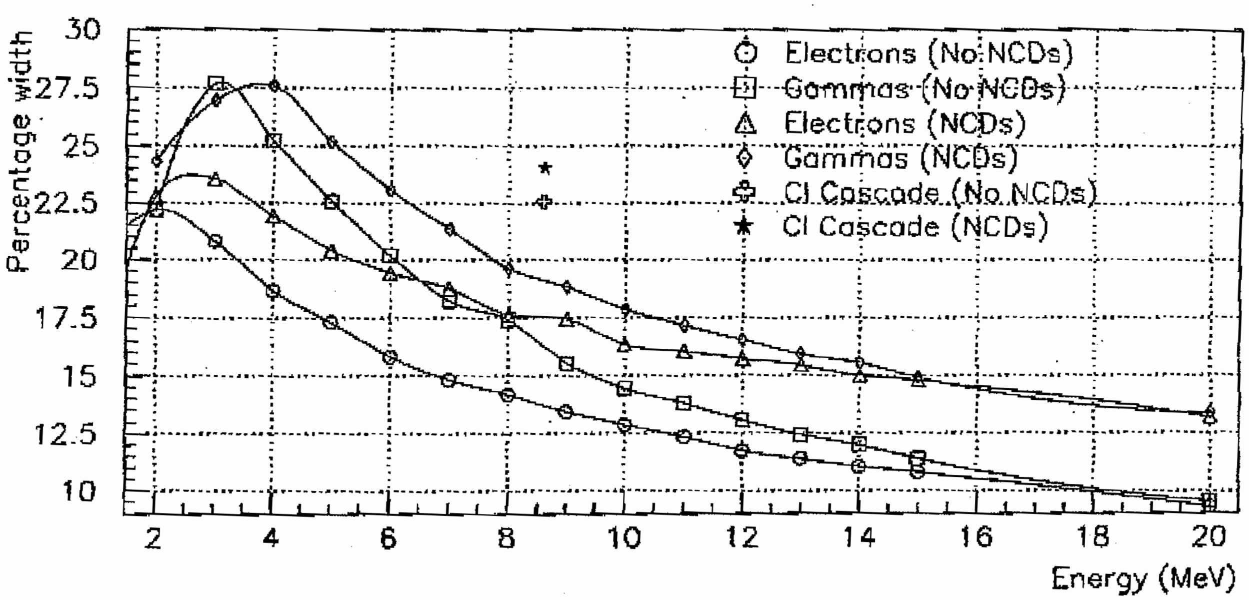

Figure 5: N_{hits} width as a function of energy for electrons and gammas created isotropically in the D_2O. The lines are merely to guide the eye and have no other significance. The drop off at low energies represents an artifact from the *10 hit cutoff*.

SNO-STR-96-055
Fitting Optical Constants in SNO Using a Pulsed N_2/Dye Laser

Richard Ford (Queen's)

March 2, 1997

Abstract

This report outlines methods under investigation to enable an ongoing monitoring of the SNO detector optical condition using the pulsed nitrogen dye laser and diffuser ball system. The absorption lengths in the D_2O, acrylic and H_2O are to be determined by extracting NHIT with various time cuts from the cumulative pmt time histograms. Bulk scattering, pmt QE and reflector condition are also to be determined from analysis of time histograms.

1 Introduction

Understanding the optical condition of the SNO detector is critical to the analysis the detector physics. The detector response to electrons, gamma rays and neutrons can only be measured at certain energies and locations and under limited conditions. Since light transmittance to the pmts is function of event position we expect to rely on Monte Carlo modeling for the analysis. Also the detector gain and response could vary unpredictably due to changes in response of the pmts or changes in the detector optical condition. These changes could include varying impurities in the water systems, deposits on the acrylic or pmt reflectors or gain and efficiency drifts in the pmts. All the optical parameters are wavelength dependent so that the Cherenkov spectrum will evolve as the light travels through the detector.

The optical parameters must be determined at several wavelengths so that this extra positional dependence is correctly modeled in the Monte Carlo (SNOMAN).

This report describes on-going work to develop techniques and analysis methods to determine and monitor critical optical parameters. The recent calibration review [4] emphasized the need for such an interim document outlining progress in the development of optical calibration procedures. This report describes how the optical parameters will be monitored by global fits to time histogram data. Another document [1] reports how some of the techniques described here will be used to perform the initial optical characterization of the SNO detector by boot strapping from air-fill data. This is important, as a measurement of the light attenuation and scattering in the acrylic tiles can only be done once during air-fill before they become complicated by covariances with light water and bulk scattering effects.

The report begins by describing the optics of the SNO detector and the uncertainty with which the optical parameters must be determined. We then describe the optical source, how the detector is triggered and the data acquisition using pmt timing histograms. Next we move through the data processing and, finally, we present procedures that are being developed for fitting to extract the optical parameters. As this work is still on-going a complete calibration run-through including global fits to all optical parameters is not yet completed. Issues dealing with the assessment of bulk scattering and the pmt concentrator reflectors are also discussed.

2 Optical Parameters

2.1 Detector Optical Parameters

To completely understand the optical response of the detector we need to be able to determine, at any time, the following optical parameters.

- Attenuation lengths of the D_2O, the acrylic and the H_2O at several wavelengths between 300nm and 450nm. We would want to know these attenuation lengths for each acrylic panel, any across panels variations and the effects of rope grooves and sanded joints[1] The attenuation

[1]As of December 1996, it seems that there likely will not be any sanded joints. All bond areas are now fine polished to aid inspections.

lengths in the water should be known at as many locations as necessary to account for possible non-homogeneous regions.

- Bulk scattering lengths (cross-sections) and the angular distributions of scattering for all detector regions and at several wavelengths.
- The position/angular response of the pmts and relative quantum efficiencies (QE) of all the pmts.
- Detector optical gain response (absolute QE).

In reality it will be impossible determine all of these parameters and distributions. Instead we must determine which parameters are important and how to measure them, and then understand any limitations this imposes on the analysis. The most critical optical parameters are the extinction coefficients (absorption plus scattering) in the detector media and the relative quantum efficiencies. By deploying the light source [2] at certain locations the separate acrylic panels and water regions can be inspected. Cuts on the pmt timing information can be used to separate out scattered and multiple-reflected light. Other sources (eg. $^{1}6$N) can provide the overall gain figure.

2.2 Parameter Uncertainty Estimates

For the laserball at the centre of the detector the D_2O attenuates the the total integrated light by a factor $e^{-\mu R}$ where R is the inner acrylic radius. For off-centre locations at radius r the attenuation is

$$\frac{I}{I_0} = \frac{1}{2}\int_{-1}^{1} \exp\left(-\mu r\cos\theta - \mu\sqrt{R^2 + (1-\cos^2\theta)}\right) d(\cos\theta) \qquad (1)$$

Evaluating this integral for various r one finds that with a D_2O attenuation length of 40m there is up to a 5% increase in light when the source is near the acrylic. If systematic shifts in the energy calibration are to be less than 1% then we want the D_2O extinction coefficient to be determined to an uncertainty of about 20%.

Now the attenuation lengths are wavelength dependent, especially near the UV, so we really want to weight the integral in equation (1) for the Cherenkov spectrum (λ^{-2}) and the pmt quantum efficiency ($QE(\lambda)$). In [6] this calculation has being done by averaging over the wavelength spectrum (see fig 1). One finds that the integral varies most rapidly for the acrylic with the inference that we need to determine the acrylic attenuation to better than 5%. For the D_2O the required uncertainty is better than 20% while for H_2O 25% uncertainty should be sufficient [6].

It is important to note the approximations assumed in [6]. Sheet-to-sheet variations in acrylic attenuation are not included. Reflections and refraction are not included, both of which would tend to increase the light variation, with the refraction effect being dependent on the acrylic attenuation. Also, we probably want to calculate these uncertainty estimates for each wavelength rather than average over the spectrum. Lastly, isotropic light is assumed while Cherenkov light is directional, thus these estimates are only true in the high statistics limits that permit a reasonable directional average for each radius. These calculations need to be performed with more detailed geometry and scattering effects using Monte Carlo (SNOMAN).

We note also that the variation in the integral (1) has the opposite sign between D_2O and acrylic, and the same sign between acrylic and H_2O. Co-variances between parameter uncertainties for the D_2O and acrylic will require care in assessing the detector positional energy dependence. This will not be as bad for co-variances between acrylic and H_2O parameter uncertainties, which is fortunate as it is known that these co-variances will exist due to some degeneracy in the light path distances. Effects due to scattering have the same sign as for acrylic attenuation (opposite to D_2O attenuation).

Measured data for the acrylic light transmission is presented in figure 2. The panel to panel variations are about 10%. In figure 3 I show the distribution of total integrated detectable light for these data for a Cherenkov source at the centre of the vessel. The Cherenkov output is multiplied by the acrylic transmission and the pmt quantum efficiency and integrated from 250nm to 600nm. The variation is about 1-2%, except that there is a tail extending to 5%. This tail is identified with the panels that have distinctly higher cutoffs[2] as seen with the distributions in figure 2.

[2] Although I have not yet tracked down the identify of all the panels, it is believed that the panels in the tail of the distribution with the higher cutoffs are from the first production runs are were used in the AV qualification wall.

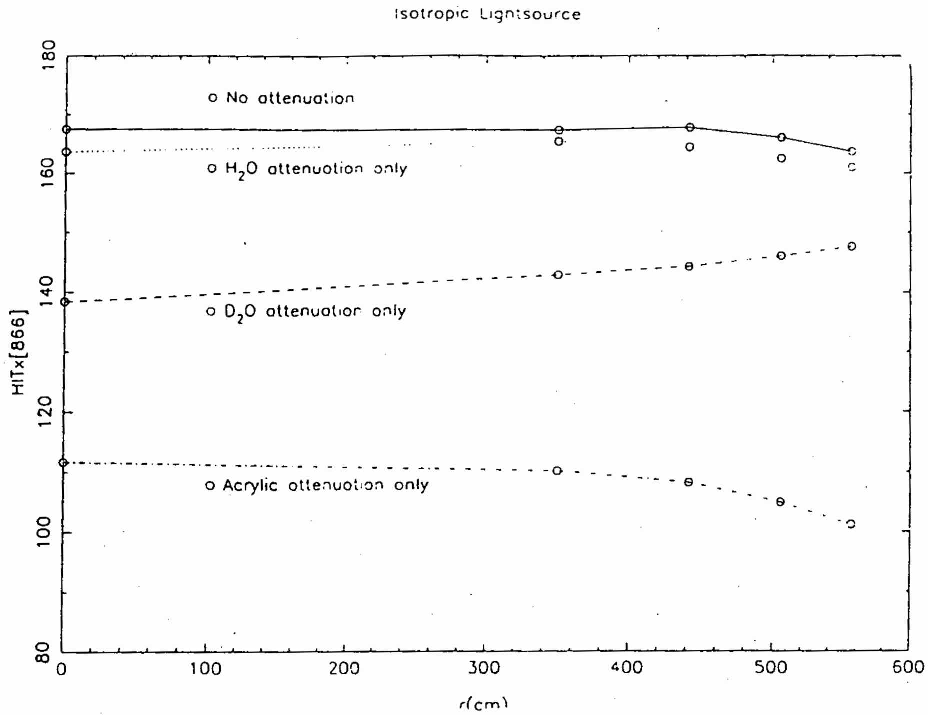

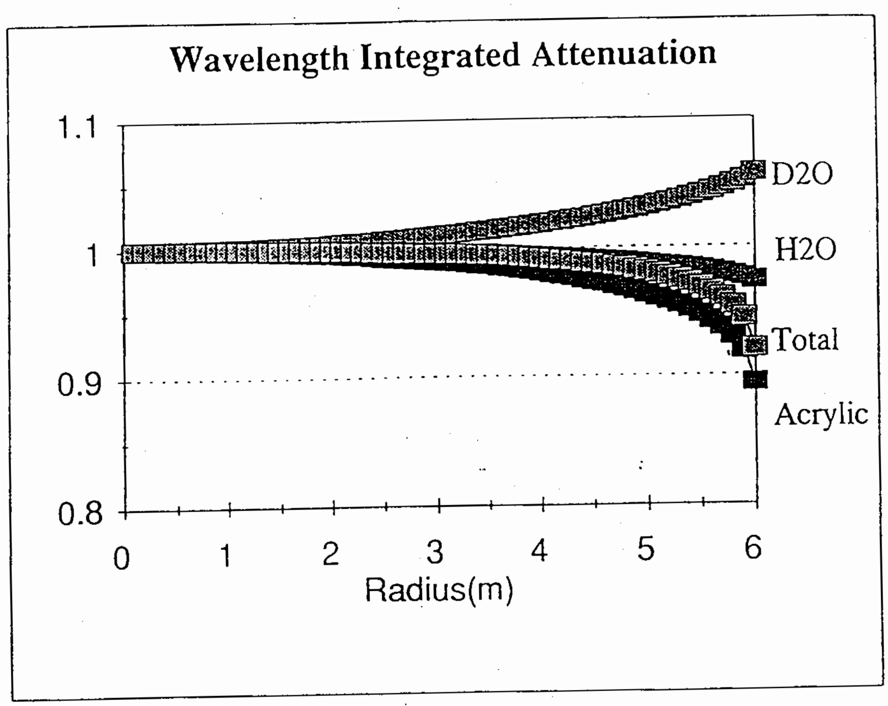

Figure 1: The upper plot is the total attenuation as a function of source radius for an isotropic light source. the secound plot is the wavelength integrated attenuation. From [6] using white book data [7].

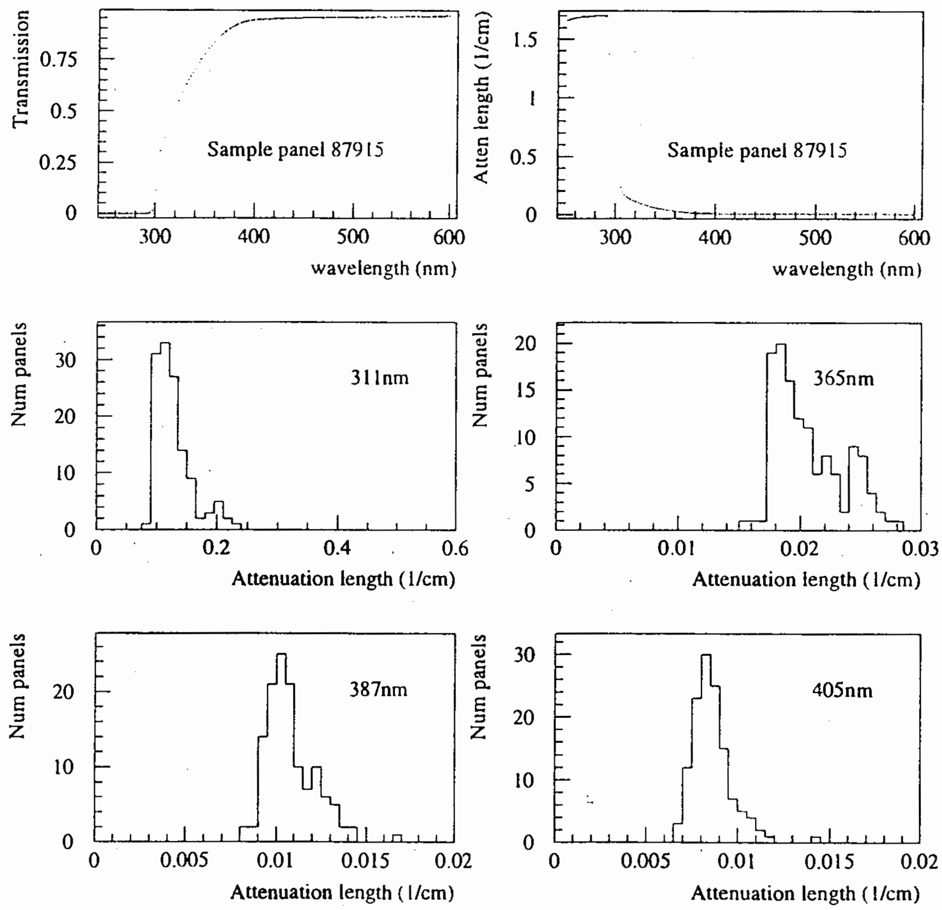

Figure 2: The top two plots show the total transmission and attenuation coefficient as a function of wavelength for a 5.84 cm acrylic panel sample. The remaining plots show the distribution of attenuations for all panels measured at various wavelengths.

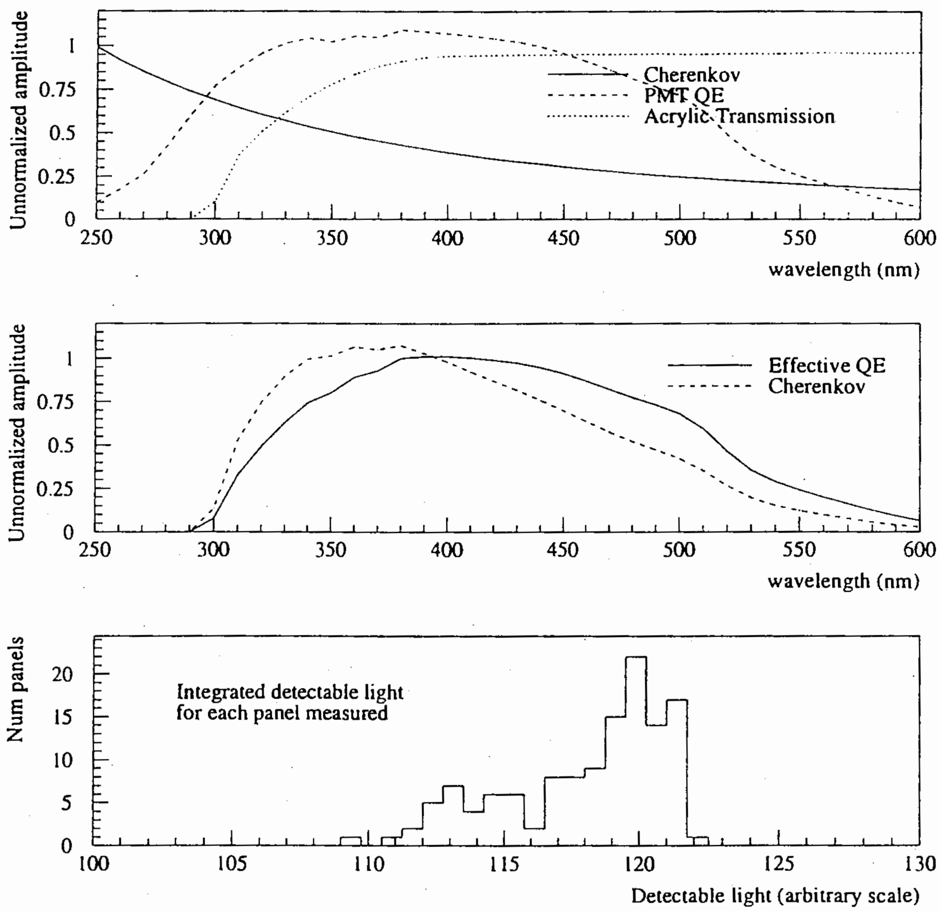

Figure 3: (a) Cherenkov output, pmt response and acrylic transmission as a function of wavelength.
(b) The solid line shows the effective QE by including the AV transmission from the data in the first plot. The dashed line is weighted by the Cherenkov spectrum.
(c) The bottom plot shows the distribution of detectable Cherenkov light by integrating over the data in plot (b) for each of the acrylic measurements. The light scale is arbitrary.